PCCP

Fronts and stationary domains during electrochemical H_2 oxidation on Pt: The impact of the position of the reference electrode on the spatiotemporal behaviour

Peter Grauel and Katharina Krischer

Fritz-Haber-Institut der Max-Planck-Gesellschaft, Faradayweg 4-6, D-14195 Berlin (Dahlem), Germany. E-mail: grauel@fhi-berlin.mpg.de, krischer@fhi-berlin.mpg.de

Received 19th February 2001, Accepted 18th April 2001
First published as an Advance Article on the web 17th May 2001

We studied the local potential distribution in front of a rotating Pt ring-electrode during hydrogen oxidation in sulfuric acid for three different positions of the reference electrode. The potential distribution was measured with a potential micro-probe. The experiments were carried out in the bistable region of the system. For large and medium distances between the reference (RE) and the working electrode (WE), transitions between the two homogeneous states occurred through nucleation and growth of the globally stable state from the initially metastable one. The transition time was considerably longer for the intermediate distance between the RE and the WE. For the closest distance used, stationary patterns formed, consisting of two domains with high and low current densities, respectively. The difference in the double layer potential of the two domains amounted to more than 1 V. The low-current density domain was covered with Pt–O whereas in the high current density domain the electrode surface consisted of 'bare' Pt. The existence of these stationary non-equilibrium structures as well as the difference of the front behaviour for the other two electrode arrangements can be traced back to the existence of a negative global coupling for intermediate and close distances between the WE and the RE.

1. Introduction

The vast majority of electrochemical reactions exhibit dynamic instabilities which manifest themselves in different nonlinear phenomena such as bistable behaviour, periodic oscillations, chaos or spatial patterns and waves.[1–4] The progress made in understanding the origin of temporal and spatial pattern formation in electrochemical systems revealed that, in general, electrochemical instabilities result from the interaction of electrode kinetics and electric properties of the entire system. For the latter the cell design is especially important, in particular the relative placement of the working (WE), counter (CE) and reference (RE) electrodes.[3–5]

For the occurrence of purely temporal instabilities, the role of the relative distance between the WE and the RE for the dynamic behaviour under potentiostatic control is meanwhile widely known. The primary dynamic instabilities, giving rise to bistability or oscillations, respectively, result from the interaction of a negative differential resistance in the current potential curve, which is characteristic for the specific electrode kinetics, and the voltage (*IR*) drop within the electrolyte between the WE and the RE.[6] Changing the position of the RE alters the dynamic behaviour of the system quantitatively or qualitatively. Thus, increasing the distance between the WE and the RE for an oscillatory system with an N-shaped current–potential curve eventually turns the oscillatory into bistable behaviour, whereas decreasing the distance, *i.e.* minimising the *IR* drop, leads finally to a stationary, monostable state.

Far less attention has been paid to the fact that spatial instabilities also depend strongly on the arrangement of the electrodes, despite several theoretical and experimental studies[5,7–14] that demonstrate the impact of the electrode arrangement on the spatiotemporal dynamics. For spatial self-organization phenomena the relative arrangement of all three electrodes matters. In general, the state of the system, which may depend on space and time, is determined by the spatial coupling among different sites of the electrode in addition to the above discussed factors defining the temporal or local dynamics. Two different modes of spatial coupling, both influenced by the cell geometry, have to be taken into account.

Firstly, different sites of the electrode are coupled through the potential distribution in the electrolyte, which also determines the migration current density 'entering the interface' at every position of the electrode. This type of spatial coupling was called migration coupling. Clearly, the potential distribution in the electrolyte depends on the overall geometry of the experiment, in particular on the arrangement of the WE and the CE. If the potential drop across the double layer changes at a certain position, this change alters the potential distribution in the entire electrolyte. Consequently, it also changes the migration current densities at the WE. Theoretical analysis showed that the closer the WE and the CE are, the smaller is the neighbourhood of a disturbance at the WE that instantaneously feels this perturbation through altered migration current densities, *i.e.*, the more localised is the coupling.[11] Systematic experiments on the influence of the relative placement of the WE and the CE on pattern formation are still missing.

The second manner by which different sites of the electrode are coupled together is caused by an electronic feedback due to the galvanostatic or potentiostatic operation mode. (For reviews of these two types of coupling in electrochemical systems see ref. 4 and 15.) Consider first the galvanostatic control. If the faradaic current at a particular position at the electrode changes, *e.g.* due to a fluctuation, the total current changes accordingly. The galvanostat provides the difference current between the actual and the set current by changing the potential of the WE. In other words, by pumping charge into the electrical double layer everywhere along the electrode.[16] Since for the temporal evolution of any location of the WE,

only the magnitude of a perturbation matters but not the position at which the perturbation occurs, the coupling represents a global coupling.

The electronic feedback in the potentiostatic case bears some similarity to the galvanostatic case. As a local change of the double layer potential, *e.g.* due to a fluctuation, leads to a redistribution of the potential in the entire electrolyte, the potential at the position of the reference electrode is also changed. Thus, the potential difference between the WE and the RE is altered, inducing an action of the potentiostat, namely a change in the potential of the WE (or equivalently the CE) until the actual and the set voltage between the WE and the RE are equal. Thereby, the interfacial potential is changed everywhere along the electrode/electrolyte interface. If the distance between every position of the WE and the RE is identical, the feedback through the potentiostat again represents a global coupling. Such a symmetric arrangement is realised if the WE is a thin annulus and the RE is located on the axis of the ring, as was the case in the studies presented here as well as in most of the earlier experimental studies.[8–10,12–14]

From the dynamic point of view, there is an important difference between the global coupling induced by the galvanostatic and the potentiostatic operation mode. In the first case, the global coupling equalises the difference between an altered average double layer potential and the local double layer potential at every position, whereas in the potentiostatic case it enhances the difference. In the first synchronising case one speaks of positive global coupling, the desynchronising coupling is called negative global coupling. For the potentiostatic operation mode, the destabilising effect is the larger, the closer the RE and the WE are. Hence, minimising the distance between the WE and the RE maximises the destabilising effect of the global coupling.

As already indicated, there are several experiments that demonstrate the pronounced effect of the position of the RE on the spatiotemporal dynamics of electrode reaction. The first observations of patterns induced by the use of a Haber–Luggin capillary that was positioned close to and in the centre of a disk or ring electrode were reported by Otterstedt *et al.* for the anodic dissolution of Co.[13] In these experiments a narrow 'active' rotating pulse with a high dissolution rate formed on an oxide-covered surface with a low reaction rate. During persulfate reduction at silver ring electrodes stationary domains with high and low reaction rates, and thus different double layer potentials were observed for a small distance between the WE and the RE.[10] In this reference, the origin of the spatial instability due to the global coupling is discussed with the help of an equivalent circuit. Christoph *et al.*[8] present a theoretical analysis of further patterns observed during Co electrodissolution.[12] Practically all patterns observed during formic acid oxidation on ring electrodes, such as standing waves and rotating pulses, also exist only when the RE and the WE are close together.[9,14,17]

In this paper we study the influence of the position of the reference electrode on pattern formation during hydrogen oxidation on Pt ring electrodes in sulfuric acid under potentiostatic control.

2. Experimental

The experimental set-up is shown in Fig. 1. A rotating Pt ring (outer diameter 30 mm, width 1 mm) embedded into a Teflon cylinder served as WE. In order to cover a large range of distances between the WE and the RE, two different configurations were used. Medium and close distances between the WE and the RE were adjusted using a J-shaped glass capillary (Haber–Luggin capillary) equipped with a Ag/AgCl electrode. The tip of the capillary was located on the axis of the WE and the distance between the tip and the plane of the WE could be

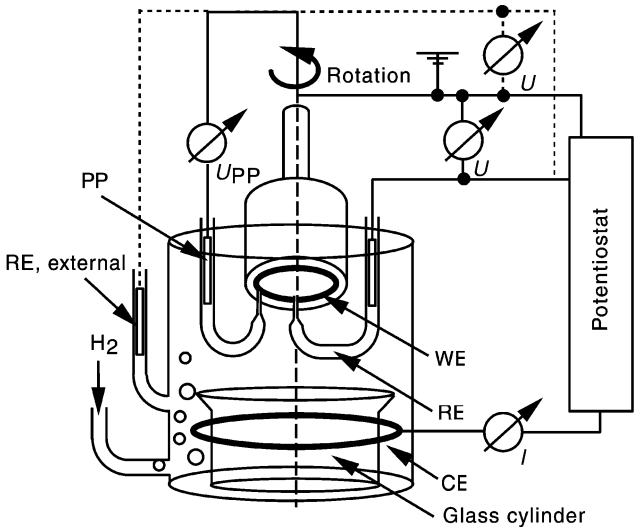

Fig. 1 Scheme of the electrochemical cell. WE: working electrode, RE: reference electrode (note that either the RE in the Haber–Luggin capillary with the tip on the axis of the ring or the external RE was used), CE: counter electrode, PP: potential probe.

adjusted from 0.3 to 13 mm $\pm$ 0.2 mm. Since for the largest distance adjustable with the capillary the above described global feedback was still present, measurements were also carried out with a Hg/Hg_2SO_4 reference electrode in a separate compartment (referred to below as 'external RE') that was connected to the main compartment about 25 mm below the plane of the WE (see Fig. 1). In this configuration the global feedback was negligible. The CE, a 1 mm thick Pt wire bent to a ring of 65 mm in diameter, was 45 mm below and parallel to the WE. In the present study, three different arrangements were employed: the external RE and the centrally placed RE with distances of 13 and 3 mm between the tip of the Haber–Luggin capillary and the WE. As determined through impedance measurements, the cell resistance for these three configurations were 290 ± 20 Ω, 212 ± 10 Ω and 176 ± 10 Ω, respectively.

To monitor the angular potential distribution in front of the WE, the tip of a second glass capillary equipped with an Ag/AgCl electrode (the potential probe, PP) was placed 1 mm $\pm$ 0.2 mm below the Pt ring. During the experiments the WE was rotated with 20 Hz, the voltage between the PP and the WE was measured with an acquisition rate of 1 kHz, which allowed us to construct a spatiotemporal picture of the potential in front of the WE. As the resistance between the PP and the WE was negligible, the measured voltage represents the local potential drop across the double layer (called double layer potential, ϕ_{DL}, below) to a good approximation.

The electrolyte consisted of a H_2-saturated (5N, Linde) 1 mM H_2SO_4 solution which was prepared from millipore water (Millipore Milli-Q water, 18 MΩ cm) and conc. H_2SO_4 (p.a., Merck). H_2 was continuously bubbled through the solution during the experiment. To prevent H_2 bubbles from accumulating at the WE, a glass cylinder was put inside the ring-shaped CE such that the H_2 bubbles rise close to the wall of the cell. The voltage between the WE and the RE was controlled by means of a potentiostat (Electronic Laboratory, Fritz-Haber-Institut). Prior to each experiment the WE was cleaned first in an ultrasonic bath and then electrochemically by oxidation–reduction cycles between -1.1 and $+1.2$ V *vs.* Hg/Hg_2SO_4 in 1 mM H_2SO_4 deaerated by N_2 (5N, Linde) for 30 min.

Results

Fig. 2a displays cyclic voltammograms of H_2 oxidation on Pt for the 3 different arrangements of the RE. The qualitative

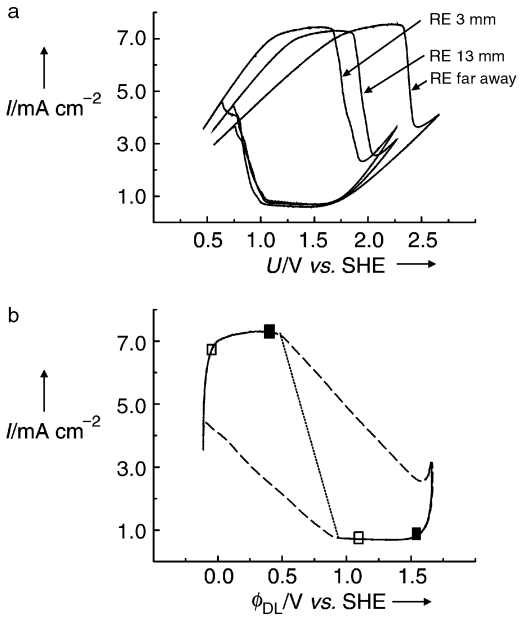

Fig. 2 (a) Cyclic voltammograms of Pt in H_2-saturated 1 mM H_2SO_4 for the three different arrangements of the RE. Scan rate: 50 mV s^{-1}. (b) Cyclic voltammogram of (a) with RE 13 mm after *IR* correction. The solid lines represent the approximate positions of the stable active (low voltage values) and passive (high voltage values) branches of the stationary current potential curve, the long-dashed lines correspond to the transitions between the branches. Note that these data suggest that the stationary current potential curve is N-shaped, the dotted line indicating the middle branch with the negative differential resistance of the N-shaped curve. This branch is unstable for the conditions of the experiment. The filled and open squares correspond to the states of the active and passive domains of Fig. 5 and 8, respectively. (The states were determined from the measured potential values.)

shape is identical in all three cases and well known. Starting at the cathodic turning point, the H_2 oxidation current increases linearly with the external voltage due to the relatively high electrolyte resistance until it has reached a diffusion limited plateau. For even more positive voltages, the current drops considerably owing to the formation of Pt–O(H) on which H_2 oxidation is strongly inhibited. On the reverse scan, the current starts to rise again when Pt–O is reduced. The difference between the three curves results from the different cell resistances for the different locations of the RE. When correcting the externally applied voltage by the *IR* drop, all three resulting current–double layer potential (I–ϕ_{DL}) plots coincide approximately. One of the *IR*-corrected cyclic voltammograms is shown in Fig. 2b.

The hystereses in the cyclic voltammograms of Fig. 2a are also found for very slow scan rates, *i.e.* under quasistationary conditions. This means that the I–U curve exhibits bistability for all three values of the cell resistance. The stable branches correspond approximately to the solid curves in Fig. 2b, whereas the dashed curves in Fig. 2b represent transient behaviour between these branches. The location of the stable states in Fig. 2b suggests that the complete I–ϕ_{DL} curve possesses a region of negative differential resistance (NDR), as indicated by the dotted line. (Note that quantitatively the potential region, in which the NDR exists under stationary conditions, might deviate somewhat from that in Fig. 2b as the data were obtained under potentiodynamic control. Note also that the width of the NDR region seems to depend on the anodic turning point, U_{max}, becoming smaller for more positive values of U_{max}. This is a result of the more irreversible nature of the oxide that forms at positive potentials.) As is the case for all bistable systems of the 'NDR-type', the bistability results from the interaction between a negative differential resistance in the I–ϕ_{DL} curve and the *IR* drop in the electrolyte.

In the following, we investigate transitions between the stable states for the three positions of the reference electrode. In particular, we demonstrate that the spatio-temporal dynamics depends qualitatively on the position of the reference electrode. This also means that whenever the spatial variable has to be taken into account, it may not be possible to obtain the dependence of the current on the 'true double layer potential' by '*IR* correction'.

For convenience, from now on we denote the high current density, low potential branch the 'active branch' and the low current density, high potential branch the 'passive branch'. First let us consider transitions from the active to the passive branch in the bistable region. In all cases, U was fixed at a value close to the positive end of the active branch, where the active state is metastable and the passive state is the globally stable one. Consequently, sooner or later, at some position a fluctuation will drive the system locally to the passive state, which will then expand at the expense of the active one. Fig. 3a shows the time trace of the total current density during such a transition for an experiment with the external RE. A comparison with the measured potential probe (PP) signal (Fig. 3b) reveals that the transition indeed does not occur homogeneously. As long as the system is in the active state, only background oscillations appear in the PP signal. They possess the rotation period and are caused by local variations of the catalytic activity of the Pt ring. However, as soon as the current density starts to decrease, the oscillations in the PP signal rise, indicating that the transition is accompanied by a nucleation and growth of the passive, oxide covered state, which possesses a considerably more positive double layer potential. Once the entire electrode has reached the passive state, the oscillation amplitude of the potential probe measurements becomes negligible, reflecting the much lower current density in the passive state. When translating the U_{PP} signal in a space-time plot, as done in Fig. 3c, nucleation and growth of the oxide phase become clearly visible. Observe the concurrence between the formation of the first oxide nucleus and the beginning of the decrease of the current density, as well as the appearance of a second oxide nucleus and the change in slope of the current–time curve (as indicated by the arrows).

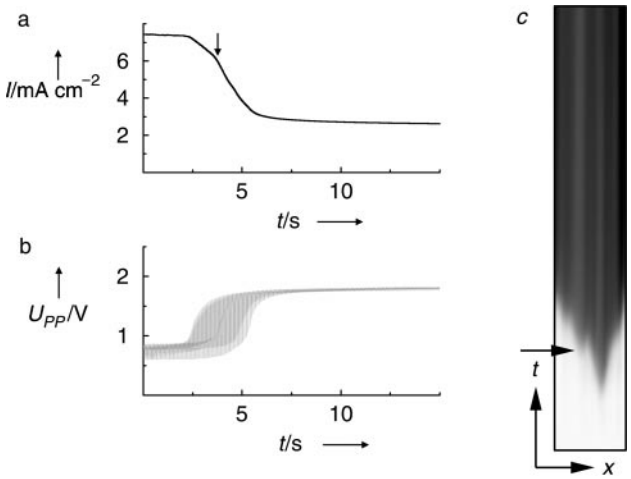

Fig. 3 Active–passive transition measured with the external RE at a constant value of the external voltage, $U = 2.35$ V *vs.* SHE. Electrolyte as in Fig. 2. (a) Current–time plot, (b) Time series of the microprobe potential (measured *vs.* SHE). (c) Position–time plot of the local double layer potential (coded in a grey scale, the largest measured potential value is shown in black, the smallest one in white). X is shown between 0° and 360°, the time axis is the same as in (a) and (b). The arrow indicates the time at which a secondary nucleation occurred.

Corresponding results for the RE at the centre and 13 mm away from the WE are shown in Fig. 4. There are two striking differences compared to the experiment with the external RE. Firstly, the duration of the transition is considerably longer. Secondly, in spite of the longer transition time, the formation of further nuclei of the oxide phase is not discernible. However, the velocity, with which the oxide phase expands, decreases, apparently in steps, during the transitions. This change in the front velocity is accompanied by a change of the slope of the $I(t)$ curve (arrows in Fig. 4a and c).

The behaviour becomes qualitatively different for the case in which the RE is placed closest to the WE, *i.e.*, when the tip of the capillary is 3 mm away from the plane of the WE (Fig. 5). The oxide phase, which again emerged due to a fluctuation, stops growing before the whole electrode is covered by oxide, leaving the electrode in a stationary, inhomogeneous state (note the different timescales in Fig. 3–5). Thus, for a close RE a stationary non-equilibrium structure forms. The difference of the double layer potential in the two domains amounts to more than 1 V. Moreover, as can be seen in Fig. 5b, the double layer potential of the active part of the inhomogeneous state is about 200 mV more negative than that of the homogeneous active state. The total current density I_{tot} of the inhomogeneous state can be roughly estimated from the size of the active and passive domains, x and $(1 - x)$, their double layer potentials, $(\phi_{DL,\,a})$ and $(\phi_{DL,\,p})$ as obtained from the potential probe measurements and the corresponding current densities available from Fig. 2a: $I_{tot} = xI_a(\phi_{DL,\,a}) + (1 - x)I_p(\phi_{DL,\,p})$. The calculated total current density compares favourably with the measured value of 3.0 mA cm^{-2}. Note that again changes in the slope of the $I(t)$ curve during the initial transient behaviour correlate with different growth velocities of the oxide phase.

The passive/active transitions measured with the three RE positions (Fig. 6–8) show qualitatively the same behaviour as the corresponding active/passive transitions. A fast transition and the formation of several nuclei occur if the RE is placed far away from the WE (Fig. 6). A much slower transition accompanied by the propagation of two fronts with somewhat different velocities is observable for an intermediate distance between the RE and the WE (Fig. 7). In contrast to the case with the external RE, here each front moves with an apparently constant velocity. Stationary fronts appear if the RE is positioned next to the WE (Fig. 8). In the latter case, an 'overshooting' of the double layer potential is also discernible: The passive domain ($\phi_{DL} = +1.10$ V) is more positive than the homogeneous passive state ($\phi_{DL} = +0.99$ V). The total current density calculated from the sizes of the domains and the measured double layer potentials (5.22 mA cm^{-2}) agrees well with the measured value (4.99 mA cm^{-2}). And again correlations between the $I(t)$ plots and the formation of nuclei or changes of front velocity are observable.

For both transitions, the active/passive and the passive/active transition, stationary structures were observed for the closest chosen distance between the RE and the WE. To determine the potential range in which these inhomogeneous structures are stable, we performed the following experiments with active and passive initial conditions: First the inhomogeneous structure was established as described above, then the external voltage was slowly scanned in the positive direction until it

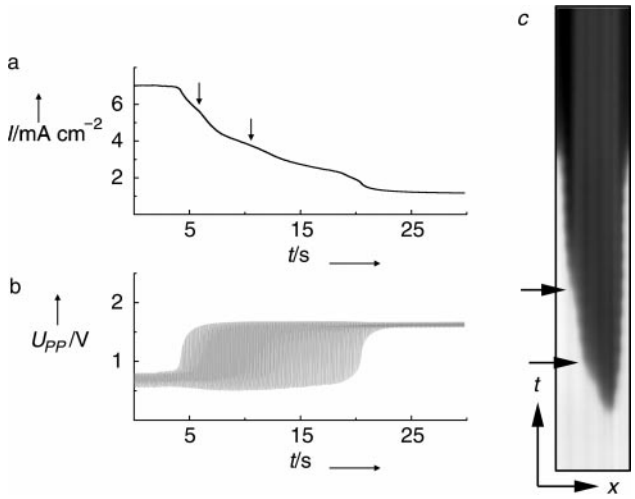

Fig. 4 Active–passive transition measured with the centrally placed RE 13 mm away from the plane of the WE. $U = 1.8$ V *vs.* SHE. Electrolyte as in Fig. 2. (a) Current–time plot, (b) time series of the microprobe potential (measured *vs.* SHE). (c) Position–time plot of the local double layer potential (coded in a grey scale, the largest measured potential value is shown in black, the smallest in white). X is shown between 0° and 360°; the time axis is the same as in (a) and (b). The arrows indicate the times at which the front velocity changed.

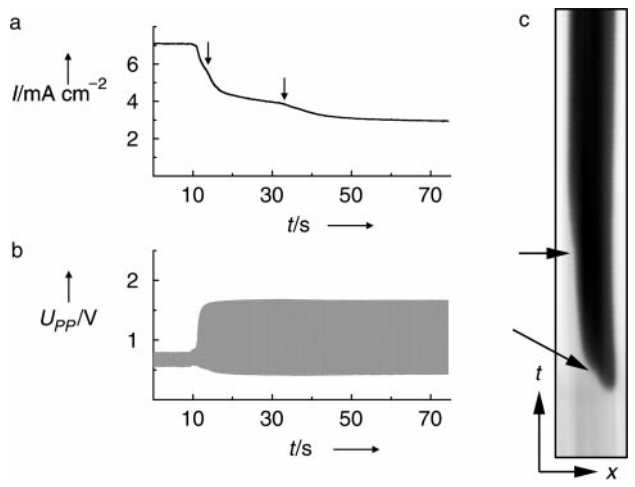

Fig. 5 Active–passive transition measured with the centrally placed RE 3 mm away from the plane of the WE. $U = 1.59$ V *vs.* SHE. Electrolyte as in Fig. 2. (a) Current–time plot, (b) time series of the microprobe potential (measured *vs.* SHE). (c) Position–time plot of the local double layer potential (coded in a grey scale, the largest measured potential value is shown in black, the smallest in white). X is shown between 0° and 360°; the time axis is the same as in (a) and (b). The arrows indicate the times at which the front velocity changed.

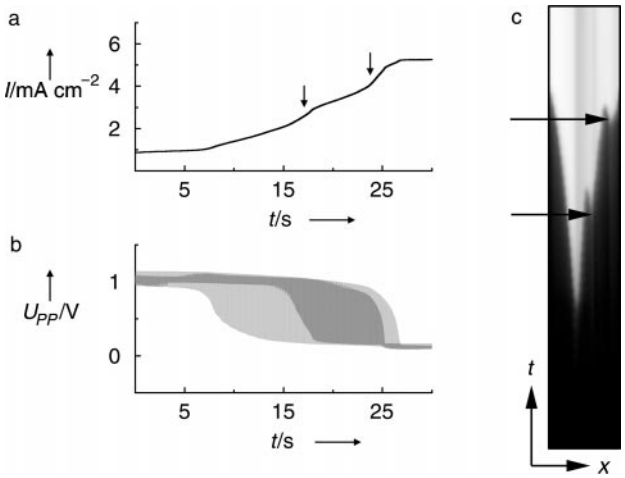

Fig. 6 Passive–active transition measured with the external RE at a constant value of the external voltage. $U = 1.25$ V *vs.* SHE. Electrolyte as in Fig. 2. (a) Current–time plot, (b) time series of the microprobe potential (measured *vs.* SHE). (c) Position–time plot of the local double layer potential (coded in a grey scale, the largest measured potential value is shown in black, the smallest in white). X is shown between 0° and 360°, the time axis is the same as in (a) and (b). The arrows indicate the times at which further nucleations of the active phase occurred.

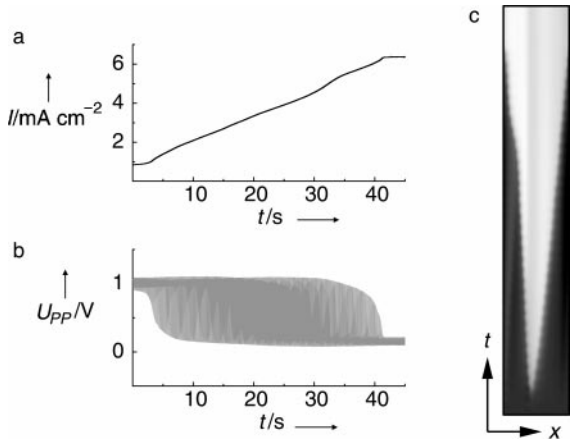

Fig. 7 Passive–active transition measured with the centrally placed RE 13 mm away from the plane of the WE. $U = 1.15$ V *vs.* SHE. Electrolyte as in Fig. 2. (a) Current–time plot, (b) time series of the micro-probe potential (measured *vs.* SHE). (c) Position–time plot of the local double layer potential (coded in a grey scale, the largest measured potential value is shown in black, the smallest in white). X is shown between 0° and 360°; the time axis is the same as in (a) and (b).

disappeared and the electrode attained again a homogeneous state. The same experiments were repeated for the negative scan direction. The experiments revealed that the stationary domains emerging from the active state belong to the same branch of inhomogeneous structures as the domains emerging from the passive state. The existence interval of the inhomogeneous solutions on the external voltage axis covers the whole

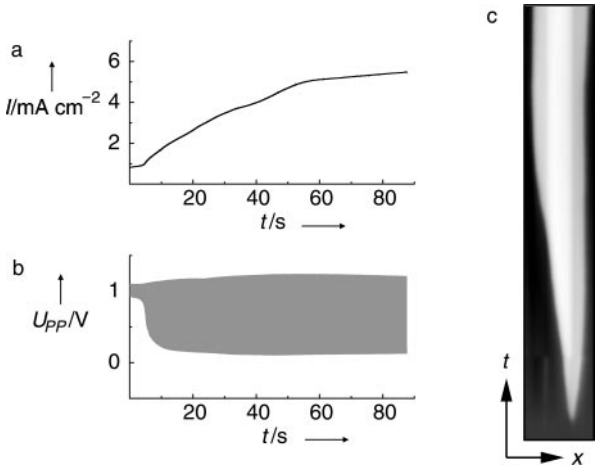

Fig. 8 Passive–active transition measured with the centrally placed RE 3 mm away from the plane of the WE. $U = 1.14$ V *vs.* SHE. Electrolyte as in Fig. 2. (a) Current–time plot, (b) time series of the micro-probe potential (measured *vs.* SHE). (c) Position–time plot of the local double layer potential (coded in a grey scale, the largest measured potential value is shown in black, the smallest in white). X is shown between 0° and 360°; the time axis is the same as in (a) and (b).

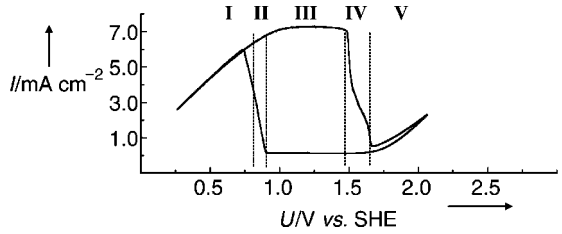

Fig. 9 Cyclic voltammogram of Pt in H_2-saturated 1 mM H_2SO_4. Distance between RE and WE: 3 mm. In regions I to V different dynamic behaviour occurs (see text). Scan rate: 5 mV s^{-1}.

range in which coexistence between the active and passive homogeneous states are observed, and extends into the respective regions where only one homogeneous state is stable. The relative sizes of active and passive domains change continuously with the external potential, whereby close to the positive end of the existence region the active domain is smallest and close to the negative end it is largest. The different dynamic regions are depicted in Fig. 9: In regions I and V the only stable state of the system is the homogeneous active or passive branch, respectively. In regions II and IV the system exhibits bistability between the respective homogeneous state and the inhomogeneous state, whereas tristability between the patterned and the two homogeneous states is found in region III.

Discussion

Qualitative[10] and quantitative[7,8] considerations on the impact of the location of the RE on the spatio-temporal behaviour revealed that whenever the RE is located at a position that does not lie on an equipotential plane parallel to the WE, a negative global coupling is introduced into the system that is the stronger the closer the RE and the WE are. The results reported here can be fully explained with these theoretical studies. In the following we give a qualitative, heuristic argument for the observed different spatio-temporal behaviours, similar to the explanation given in two recent review articles.[4,15] For quantitative aspects we refer to ref. 7 and 8.

Consider first the case of the external reference electrode, where comparatively fast transitions between the two homogeneous stationary states were observed. For this large distance between WE and RE the negative global coupling can be neglected and the transitions in the bistable region result from the interaction of reaction dynamics and migration coupling: Depicted in Fig. 10 is a schematic of a transition in the bistable region in the presence of migration coupling. The two stable states possess double layer potentials $\phi_{DL,1}$ and $\phi_{DL,3}$ respectively, and are separated by the (unstable) saddle point at $\phi_{DL,2}$. For homogeneous situations the system is driven towards state 1 whenever ϕ_{DL} is lower than $\phi_{DL,2}$ and towards state 3 whenever it is higher. However, state 3 is the globally stable one. Thus, as long as the system is in state 1, eventually a small nucleus of state 3 will be born through an overcritical fluctuation (solid curve in Fig. 10), thereby generating a potential gradient parallel to the interface. This potential gradient modifies the potential distribution in the electrolyte, and in particular, it alters the migration currents at the interface. The arrows below the potential profile in Fig.

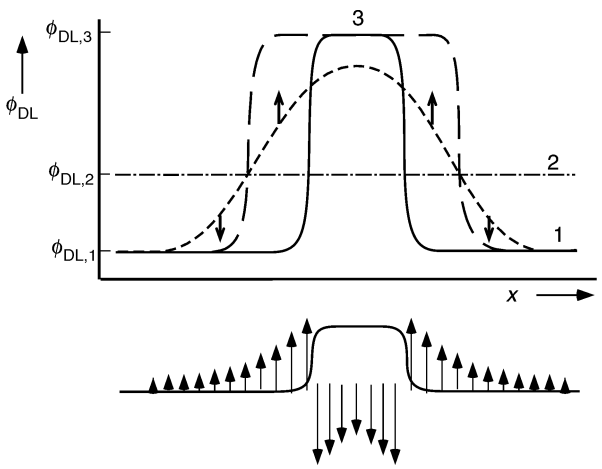

Fig. 10 Top: Development of a front in bistable electrochemical systems by interaction of the dynamic of the homogeneous system and migration coupling. Bottom: Strength and sign of migration coupling for a potential profile as shown above (solid line).

10 indicate the strength of the migration coupling as a function of position. Due to the action of this migration coupling alone, the potential distribution would become flatter (short dashed line), finally leading again to a homogeneous state. However, the dynamics of the homogeneous system drives all locations with a double layer potential above $\phi_{DL,2}$ towards $\phi_{DL,3}$ and all states below $\phi_{DL,2}$ to $\phi_{DL,1}$. Hence, the concerted action of the local dynamics and the migration coupling results in the expansion of state 3 whereby a front or moving interface forms (*cf.* Fig. 3 and 6). States on the interface are closer to the separatrix than the homogeneous states. Consequently, for those states a smaller fluctuation, which is more likely to occur than a larger one, is sufficient to drive the system to state 3. As migration coupling is long-range,[11] the extension of the interface cannot be neglected in comparison to the total length of the system, *i.e.* the circumference of the WE. The width of the interface together with the closer distances of interface states to the separatrix lead to a larger nucleation rate of the globally stable state from the inhomogeneous state than from the homogeneous state. This explains the observation of additional nuclei of the passive (*cf.* Fig. 3) or the active (*cf.* Fig. 6) state during the comparatively short time of the transition in the experiments (*cf.* Fig. 3 and 6).

Assume now that we create an identical initial condition (solid line, Fig. 10) in the presence of negative global coupling. Then the average double layer potential is larger than that of the homogeneous stable state 1 and smaller than that of state 3, and the negative global coupling drives all states in state 1 towards even smaller values of ϕ_{DL} and those in state 3 towards still larger potentials. With the help of Fig. 2b it is straightforward to see that if these potential values represented stationary states they would lie further inside the bistable region where the active state is more stable than our initially active homogeneous steady state (as measured from the distance to the separatrix) and the passive state less stable than the initially passive homogeneous state. Because the front velocity, or equivalently the growth rate of the globally stable state, is proportional to the difference in the relative stabilities of both states,[18] the front motion is slowed down, as observed in the experiments with intermediate distance of the RE (Fig. 4 and 7). If the strength of the global coupling exceeds a critical value, the shift of states 1 and 3 towards smaller and larger values of ϕ_{DL}, respectively, becomes so pronounced that eventually a state with equally stable active and passive regions is established. Hence the front motion stops, creating an inhomogeneous structure consisting of two domains (*cf.* Fig. 5 and 8). This illustrative picture also makes plausible, why secondary nuclei were practically not observed for intermediate or close RE (*cf.* Fig. 4, 5, 7 and 8). The probability for an overcritical local fluctuation to occur becomes smaller as the distance between the interfacial states and the separatrix (state 2) becomes larger.

Note that for N-shaped current–potential curves the formation of inhomogeneous domains in the presence of global coupling is not restricted to parameter values where the homogeneous system exhibits bistability. Rather, the domains may also form when load line and polarization curve possess only one intersection that lies on the NDR branch of the polarization curve.[7,10]

Before global coupling and its impact on the dynamic behaviour was discussed in electrochemical systems, it was proven to give rise to interesting pattern formation in other disciplines, such as semiconductor physics,[19–24] gas discharge devices,[25] or catalytic exothermic reactions.[26–31] The existence of stationary domains was also found in these systems and was attributed to the stabilisation of the equistability condition of a bistable system in a wide parameter region.[32]

Conclusion

The presented spatially resolved investigations of a reaction, which is certainly among those whose global behaviour is most studied, represent a further example of how important it is to be aware of possible spatial instabilities when interpreting globally assembled electrochemical data. This holds in particular when a Haber–Luggin capillary is used.

Acknowledgements

We thank H. Varela and W. Vielstich for fruitful discussions. Financial support by the Deutsche Forschungsgemeinschaft under SFB 555 is gratefully acknowledged.

References

1 J. L. Hudson and T. T. Tsotsis, *Chem. Eng. Sci.*, 1994, **49**, 1493.
2 M. T. M. Koper, *Adv. Chem. Phys.*, 1996, **92**, 161.
3 K. Krischer, in *Modern Aspects of Electrochemistry*, ed. B. E. Conway, J. O. M. Bockris and R. White, Kluwer Academic/Plenum publishers, New York, 1999.
4 K. Krischer, *J. Electroanal. Chem.*, 2001, **501**, 1.
5 A. Birzu, B. J. Green, R. D. Otterstedt, N. I. Jaeger and J. L. Hudson, *Phys. Chem. Chem. Phys.*, 2000, **2**, 2715.
6 M. T. M. Koper, *Electrochim. Acta*, 1992, **37**, 1771.
7 J. Christoph, PhD Thesis, FU Berlin, Berlin, 1999.
8 J. Christoph, R. D. Otterstedt, M. Eiswirth, N. I. Jaeger and J. L. Hudson, *J. Chem. Phys.*, 1999, **110**, 8614.
9 J. Christoph, P. Strasser, M. Eiswirth and G. Ertl, *Science*, 1999, **284**, 291.
10 P. Grauel, J. Christoph, G. Flätgen and K. Krischer, *J. Phys. Chem. B*, 1998, **102**, 10264.
11 N. Mazouz, G. Flätgen and K. Krischer, *Phys. Rev. E*, 1997, **55**, 2260.
12 R. D. Otterstedt, N. I. Jaeger, P. J. Plath and J. L. Hudson, *Chem. Eng. Sci.*, 1999, **54**, 1221.
13 R. D. Otterstedt, P. J. Plath, N. I. Jaeger and J. L. Hudson, *J. Chem. Soc., Faraday Trans.*, 1996, **92**, 2933.
14 P. Strasser, J. Christoph, W.-F. Lin, M. Eiswirth and J. L. Hudson, *J. Phys. Chem. B*, 2000, **104**, 1854.
15 K. Krischer and N. Mazouz, *Angew. Chem.*, 2001, **113**, 842; K. Krischer, N. Mazouz and P. Grauel, *Angew. Chem. Int. Ed. Engl.*, 2001, **40**, 850.
16 N. Mazouz, G. Flätgen, K. Krischer and I. G. Kevrekidis, *J. Electrochem. Soc.*, 1998, **145**, 2404.
17 Y. Lee, P. Strasser, J. Christoph, M. Eiswirth and G. Ertl, *J. Chem. Phys.*, 2001, in press.
18 A. S. Mikhailov, *Foundations of Synergetics I*, Springer, New York, 1994.
19 E. Schöll, *Nonequilibrium Phase Transitions in Semiconductors*, Springer, Berlin, 1987.
20 A. Martin, M. Lerch, P. Simmonds and L. Eaves, *Appl. Phys. Lett.*, 1994, **64**, 1248.
21 A. Alekseev, S. Bose, P. Rodin and E. Schöll, *Phys. Rev. E*, 1998, **57**, 2640.
22 M. Meixner, P. Rodin and E. Schöll, *Phys. Rev. E*, 1998, **58**, 5586.
23 M. Meixner, P. Rodin and E. Schöll, *Phys. Rev. E*, 1998, **58**, 2796.
24 M. Meixner, P. Rodin, E. Schöll and A. Wacker, *Eur. Phys. J. B*, 2000, **13**, 157.
25 H. Willebrand, T. Hüntler, F. J. Niedernostheide, R. Dohmen and H.-G. Purwins, *Phys. Rev. A*, 1992, **45**, 8766.
26 V. Barelko, I. I. Kurochka, A. G. Merzhanov and K. G. Shkadinskii, *Chem. Eng. Sci.*, 1977, **33**, 805.
27 V. V. Barelko, V. M. Beibutyan, Y. V. Volodin and Y. B. Zeldovich, *Dokl. Akad. Nauk SSSR*, 1981, **257**, 339.
28 Y. E. Volodin, V. V. Barelko and A. G. Merzhanov, *Sov. J. Chem. Phys.*, 1982, **5**, 1146.
29 U. Middya and D. Luss, *J. Chem. Phys.*, 1994, **100**, 3568.
30 M. A. Liauw, M. Somani, J. Annamalai and D. Luss, *AIChE J.*, 1997, **43**, 1519.
31 J. Annamalai, M. Liauw and D. Luss, *Chaos*, 1999, **9**, 36.
32 For an introduction to pattern formation in the presence of global coupling see ref. 18.